


Low-Frequency Imaginary Impedance at the Superconducting Transition of $2H\text{-NbSe}_2$

David Perconte,¹ Samuel Mañas-Valero^{1,2}, Eugenio Coronado^{1,2}, Isabel Guillamón^{1,3} and Hermann Suderow^{1,3,*}

¹*Departamento de Física de la Materia Condensada, Laboratorio de Bajas Temperaturas y Altos Campos Magnéticos, Instituto Nicolás Cabrera and Condensed Matter Physics Center (IFIMAC), Universidad Autónoma de Madrid, Madrid E-28049, Spain*

²*Instituto de Ciencia Molecular (ICMol), Universidad de Valencia, Catedrático José Beltrán 2, Paterna 46980, Spain*

³*Unidad Asociada de Bajas Temperaturas y Altos Campos Magnéticos, UAM, CSIC, Cantoblanco, Madrid E-28049, Spain*

 (Received 6 November 2019; revised manuscript received 6 April 2020; accepted 13 April 2020; published 18 May 2020)

The superconducting transition leads to a sharp resistance drop in a temperature interval that can be a small fraction of the critical temperature T_c . A superconductor exactly at T_c is thus very sensitive to all kinds of thermal perturbation, including the heat dissipated by the measurement current. We show that the interaction between electrical and thermal currents leads to a sizable imaginary impedance at frequencies of the order of tens of hertz at the resistive transition of single crystals of the layered material $2H\text{-NbSe}_2$. We explain the result using models developed for transition-edge sensors. By measuring under magnetic fields and at high currents, we find that the imaginary impedance is strongly influenced by the heat associated with vortex motion and out-of-equilibrium quasiparticles.

DOI: [10.1103/PhysRevApplied.13.054040](https://doi.org/10.1103/PhysRevApplied.13.054040)

I. INTRODUCTION

Since the discovery of superconductivity by Kamerlingh Onnes over a century ago, the resistive transition has continued to fascinate researchers, in spite of now being a routine measurement in many laboratories all over the world. The transition is often very sharp, which allows one to build extremely sensitive thermometers from superconductors stabilized at T_c . These are called transition-edge sensors (TESs) and are used in x-ray and γ -ray detection [1–3].

However, this implies that heat dissipation has to be considered very carefully at the transition. There is usually no imaginary component in the impedance of a superconductor at low frequencies. But an ac signal inevitably produces a time-varying temperature in the superconductor when its resistance is finite close to T_c . This leads to an imaginary component in the impedance, which depends on the

thermal circuit describing the connection of the superconductor with its environment [1]. While this has long been known and is routinely used to characterize TESs [1,4–6], it has received little attention in studies of the resistive transition in superconducting compounds [7,8].

The techniques for studying the resistive transition in a superconductor are numerous, but are mostly restricted to electrical measurements [7,8]. There are, however, some relevant open questions, which require an additional tool that provides access to the thermal properties. Close to the transition, Cooper pairs coexist with normal quasiparticles in an out-of-equilibrium quantum liquid whose thermal behavior is still largely unknown [9–12]. The usual specific-heat-capacity measurements are made with zero applied current through the sample, and an external heater and thermometer. When a current through the sample is applied close to T_c , the sample dissipates heat, and it can be quite difficult to measure the temperature with an external thermometer. But at the resistive transition, the sample is itself both a heater and a thermometer. We show below that imaginary-impedance measurements can be used as a thermal probe of the superconducting transition.

We make detailed measurements of the real and imaginary impedance of a $2H\text{-NbSe}_2$ single crystal. We study a large imaginary component in the impedance at the transition and measure the temperature dependence of the

*hermann.suderow@uam.es

Published by the American Physical Society under the terms of the [Creative Commons Attribution 4.0 International](https://creativecommons.org/licenses/by/4.0/) license. Further distribution of this work must maintain attribution to the author(s) and the published article's title, journal citation, and DOI.

imaginary component as a function of frequency, magnetic field, and applied current. We take expressions for the heat and current flow developed for TESs and use these successfully to reproduce our results. We show that He exchange gas modifies the thermal connection, and characterize it using the imaginary component. We also obtain the temperature dependence of the specific heat capacity close to the transition. For small applied currents, we find a result compatible with macroscopic specific-heat-capacity experiments, with a peak at T_c of the order of the electronic contribution to the specific heat capacity. Under magnetic fields and with large currents, we find an increased peak, suggesting that vortex motion and out-of-equilibrium quasiparticles influence the heat balance.

II. EXPERIMENT AND METHODS

$2H\text{-NbSe}_2$ crystals are grown by iodine vapor transport. The crystals display the usual properties of $2H\text{-NbSe}_2$: a feature at the charge-density-wave transition in the resistivity, a T_c of about 7.2 K, and a residual resistance ratio above 30, which gives an electronic mean free path above 100 nm (well above the superconducting coherence length of approximately 10 nm) [13]. We thin down a $2H\text{-NbSe}_2$ single crystal by exfoliation to about 14 μm thickness and glue the sample onto a copper sample holder. The sample is 1.6 mm long and 0.8 mm wide, and we use a thin layer of Kapton to separate it electrically from the sample holder. We use carefully thermalized twisted-pair wires on a pumped helium-bath cryostat equipped with a superconducting coil and a temperature controller. We measure the impedance using a lock-in amplifier and carefully monitor the phase shift and its temperature dependence. The highest applied currents correspond to a current density of about 2×10^6 A/m², which is five orders of magnitude below the depairing current density $J_d \approx 10^{11}$ A/m² [14]. The power used is about 50 μW at the largest currents.

We describe schematically our electrical and thermal circuits in Fig. 1. The current flows through the resistance of the sample and the wires [with resistance R_{cir} and inductance L_{cir} , Fig. 1(a)]. The inductance L_{cir} is of the order of a few microhenries, and R_{cir} is much smaller than the resistance of the sample. The voltage induced by the oscillatory current is given by $L(dI/dt)$ (where L is the sum of the inductance of the wiring and the kinetic inductance L_K of the sample). This equals the voltage drop across the sample, ZI , plus the voltage drop across the resistances in the circuit [1–3,15,16]:

$$-L \frac{dI}{dt} = (R_{\text{source}} + R_{\text{cir}})I + ZI. \quad (1)$$

A time-dependent current in the sample produces a time-dependent temperature in the sample too. The Joule power $P_{\text{elec}} = RI^2$ released in the sample [with $R = \text{Re}(Z)$], minus the power leaking through the thermal link to the

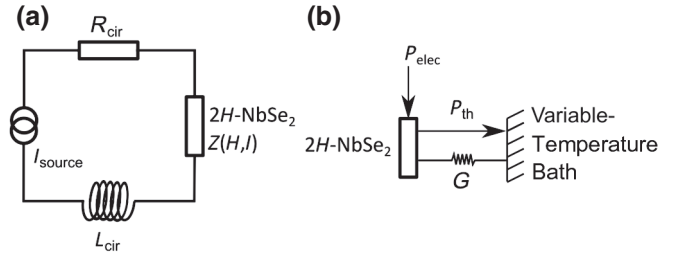


FIG. 1. (a) Electrical scheme of our setup. A current source (I_{source}) is connected to the $2H\text{-NbSe}_2$ sample, with impedance Z , through wiring that has a finite resistance R_{cir} and an inductance L_{cir} . $I(t)$ follows Eq. (1). (b) Thermal scheme. An electrical power P_{elec} is introduced by an electrical current in the $2H\text{-NbSe}_2$ sample (box). This produces heat that flows to the thermal bath (P_{th}) through the thermal connection G . $T(t)$ follows Eq. (2) and is connected to $I(t)$ through $P_{\text{elec}} = RI(t)^2$.

bath, P_{th} [Fig. 1(b)], is equal to the power that the sample absorbs, which is the heat capacity C of the sample times dT/dt [1–3,15,16]:

$$C \frac{dT}{dt} = RI^2 - P_{\text{th}}. \quad (2)$$

We introduce the parameters $\alpha = (T/R)(\partial R/\partial T)$ and $\beta = (I/R)(\partial R/\partial I)$, which are the logarithmic derivatives of $R = \text{Re}(Z)$ with respect to the temperature and current [1–3,15,16], and perform a local linearization to write the impedance versus frequency, $Z(\omega)$, as follows:

$$Z(\omega) = i\omega L + R_{\text{cir}} + R(1 + \beta) + \frac{2 + \beta}{1 + i\omega \frac{CT}{GT - I^2 R \alpha}} \frac{R^2 I^2 \alpha / (GT)}{1 - \frac{I^2 R \alpha}{GT}}. \quad (3)$$

The reactance is the imaginary part of Z , $\text{Im}(Z)$:

$$\text{Im}(Z)(\omega) = \omega L - \omega \frac{CT(2 + \beta)}{1 + \left| \omega \frac{CT}{GT - I^2 R \alpha} \right|^2} \frac{R^2 I^2 \alpha / (GT)^2}{\left(1 - \frac{I^2 R \alpha}{GT} \right)^2}. \quad (4)$$

The parameters T , R , I , and α are measured, whereas β , G , and C are determined by comparing the measured $\text{Im}(Z)(\omega)$ with this expression. The reactance has a maximum at a frequency of $(GT - I^2 R \alpha)/CT = G/C - I^2 dR/C dT$, which is the difference between the inverse of the thermal time constant of the system, G/C , and the ratio between the differential Joule power, $P_{\text{elec}} = I^2 dR$, and the differential power admitted by the sample, $C dT$.

III. RESULTS AND DISCUSSION

In Figs. 2(a) and 2(b), we show the real and imaginary impedance. At zero magnetic field (blue curves), we observe a very sharp transition in the real impedance. We

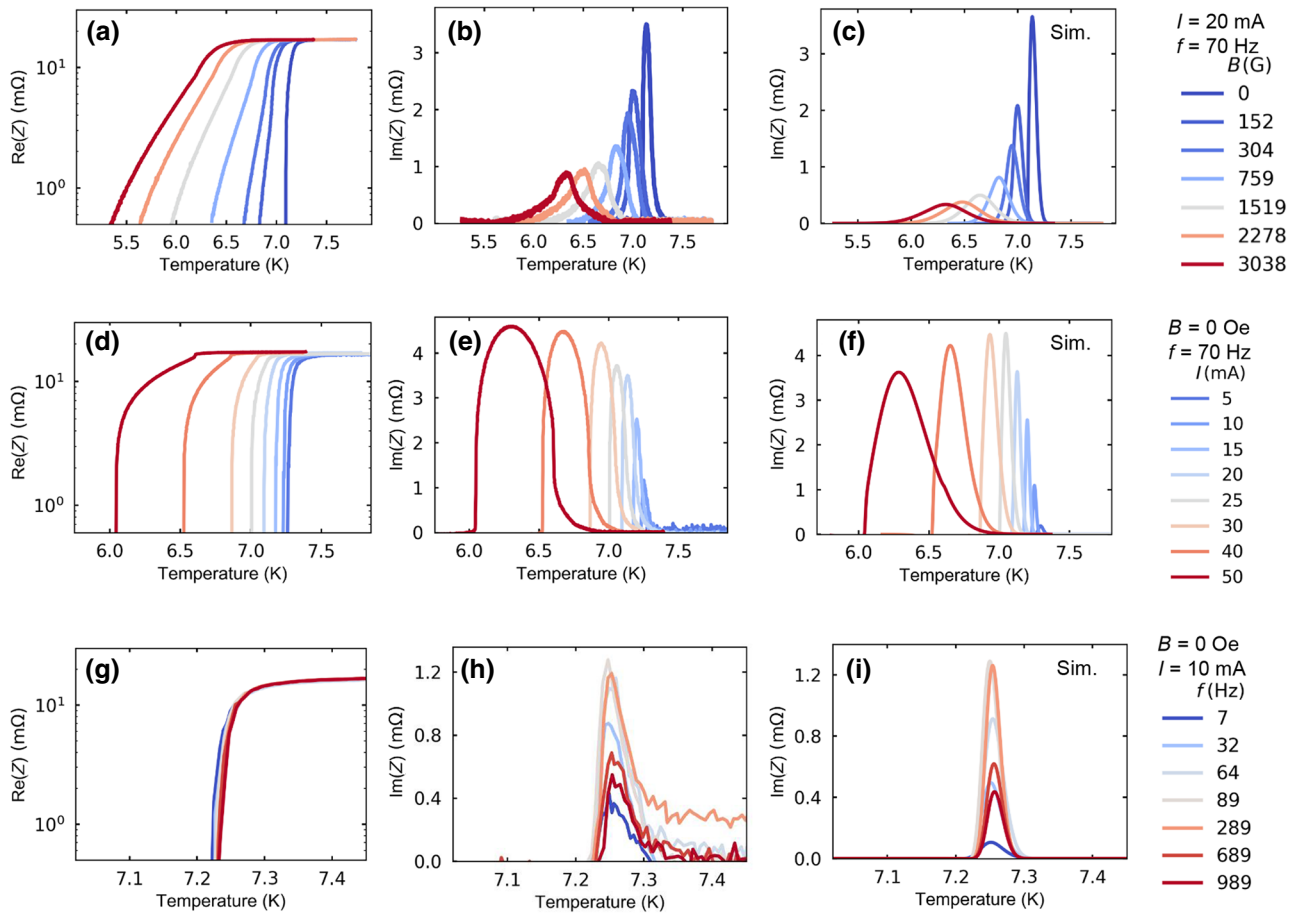


FIG. 2. (a) Real impedance versus temperature for different magnetic fields (lines from blue to red, 0, 152, 304, 759, 1519, 2278, and 3038 Oe). (b) Imaginary impedance versus temperature for the same magnetic fields. The data in (a),(b) are taken at 20 mA and a frequency of 70 Hz. (d) Real impedance for different values of the current (from blue to red, 5, 10, 15, 20, 25, 30, 40, and 50 mA). (e) Imaginary impedance versus temperature for the same values of current. The data in (d),(e) are taken at zero magnetic field and a frequency of 70 Hz. (g) Real impedance versus temperature for different frequencies (from blue to red, 7, 32, 64, 89, 289, 689, and 989 Hz). (h) Imaginary impedance for the same frequencies. The data in (g),(h) are taken at zero magnetic field and a current of 20 mA. (c),(f),(i) Imaginary impedance obtained using Eq. (4) and the approximations described in the text. For clarity, we show the color scale used in each set of figures as bars on the right.

observe, at the same time, a strong sharp peak in the imaginary impedance. The magnetic field reduces the superconducting critical temperature and broadens the resistive transition [Fig. 2(a)]. The decay of the real impedance with temperature is exponential for low values of the impedance. The imaginary impedance decreases, and the peak is broader than at zero field.

In Figs. 2(d) and 2(e), we show the effect of increasing the current at zero field. We observe that the transition in the real impedance broadens. The peak in the imaginary impedance, however, strongly increases in size, reaching approximately 30% of the value of the real impedance. The temperature range in which the real impedance is high corresponds to a broad peak in the imaginary impedance. The imaginary impedance vanishes exponentially at low temperatures, following the real impedance.

In Figs. 2(g) and 2(h), we show the effect of modifying the frequency at a fixed current and zero magnetic field. The real impedance remains unaffected, but the imaginary impedance first increases up to about 70 Hz and then decreases as 1 kHz is approached. Thus, there is a frequency range, of the order of a few tens of hertz, where the imaginary impedance is at its largest. In Appendix A, we present the imaginary part of the impedance at a fixed point in the transition as a function of frequency.

Let us start by discussing the usual electrodynamic frequency response of superconductors. The kinetic inductance L_K provides a finite reactance in the superconducting phase [17]. We can estimate the kinetic inductance L_K using $L_K = (4\pi\lambda^2)/d = 3.6 \times 10^{-8}$ H, where $\lambda = 200$ nm is the penetration depth of 2H-NbSe₂[18] and d is the thickness of the sample. This provides a contribution to

the reactance three orders of magnitude below our observations, of 3.6×10^{-3} m Ω at 100 Hz. Furthermore, the maximum of the kinetic inductance occurs at frequencies in the gigahertz range, whereas we work here at frequencies well below a kilohertz, and the maximum of the reactance occurs at merely 70 Hz [Figs. 2(h) and 2(i)]. Thus, the kinetic inductance does not explain the observed behavior.

We can also calculate the thermal-diffusion length scale $L_{\text{thermal}} = \kappa/C\tau\rho$ (where κ is the thermal conductivity of the sample, τ is the time scale of the variations in the current, and ρ is the density) and see that it is much larger than the sample size (it is about 3 mm at 70 Hz and 1 cm at 1 Hz). Thus, there are no temperature gradients induced within the sample by the applied current.

We now consider the coupling between electronic and heat transport, using the model described previously and Eq. (4). We start with a temperature-independent heat capacity $C = 2.8 \times 10^{-7}$ J/K and a temperature-independent thermal conductance $G = 2.8 \times 10^{-4}$ W/K, and we assume a temperature-independent parameter $\beta = 0.4$. In most of the temperature and current range we are considering, the I - V characteristics of NbSe₂ are in the vortex-liquid or flux-flow regime, which leads to a smooth nonexponential behavior. Furthermore, we start by taking for $d\text{Re}(Z)/dT$ versus temperature a Gaussian form centered at the midpoint of the transition. We replace R in Eq. (4) with the measured impedance. We can then calculate the reactance using Eq. (4). We obtain the results shown in Figs. 2(c), 2(f), and 2(i). The orders of magnitude of the imaginary impedance and of its temperature dependence are similar to those observed in the experiment [Figs. 2(b), 2(e), and 2(h)].

We thus see that the broadening of the transition in the real impedance $\text{Re}(Z)$ obtained as a function of the magnetic field [Fig. 2(a)] results in a strong decrease in the imaginary impedance $\text{Im}(Z)$ [Fig. 2(b)] at the transition. On the other hand, an increase in the current I , with a concomitant broadening of the transition in the real impedance $\text{Re}(Z)$, produces the opposite effect in the imaginary impedance $\text{Im}(Z)$. $\text{Im}(Z)$ [Fig. 2(e)] increases strongly with the current. Finally, as a function of frequency, we find that the imaginary impedance $\text{Im}(Z)$ shows a peak at about 70 Hz and vanishes at low and high frequencies, as also discussed in more detail in Appendix A. Thus, the order of magnitude of the effect is very well captured by the thermal model, in spite of the approximations used.

Let us now discuss the dependence as a function of the pressure of the exchange gas, shown in Fig. 3. Usually, exchange gas improves the coupling of the sample to its thermal environment. It thus primarily increases the thermal conductivity G . Interestingly, the imaginary impedance $\text{Im}(Z)$ provides a rather accurate account of the exchange gas present in the experiment. To see this, we measure $\text{Im}(Z)(\omega)$ as a function of the frequency for

different exchange-gas residual pressures. The frequency dependence for vanishing exchange-gas pressure follows that observed in Figs. 2(g) and 2(h) and discussed in Appendix A. We use our model to obtain G for each value of exchange-gas pressure.

Figure 3(a) displays the thermal conductance G obtained versus the He exchange-gas pressure. In Fig. 3(b), we show $\text{Im}(Z)(\omega)$ for different exchange-gas pressures. We observe that $\text{Im}(Z)(\omega)$ decreases strongly with increasing exchange-gas pressure. It is thus a good measurement of the residual exchange gas present in the experiment. The frequency dependence $\text{Im}(Z)(\omega)$ calculated using our model, changing the value of G , is shown in Fig. 3(c). We see that the calculations provide a good account of the observed overall decrease in $\text{Im}(Z)(\omega)$. There are some aspects, such as the dependence of the position of the maximum with respect to frequency, that are not precisely captured by the model. Nevertheless, it is quite remarkable that the values of G , as well as its dependence on the residual exchange-gas pressure, are in agreement with direct measurements of the thermal conductance of the He exchange gas [19]. Thus, the improved heat transport to the thermal bath through convection by the exchange gas clearly leads to a thermal behavior of the sample that is less influenced by small oscillations in temperature.

We also see that there are slight differences between the calculated [Figs. 2(c), 2(f), and 2(i)] and measured

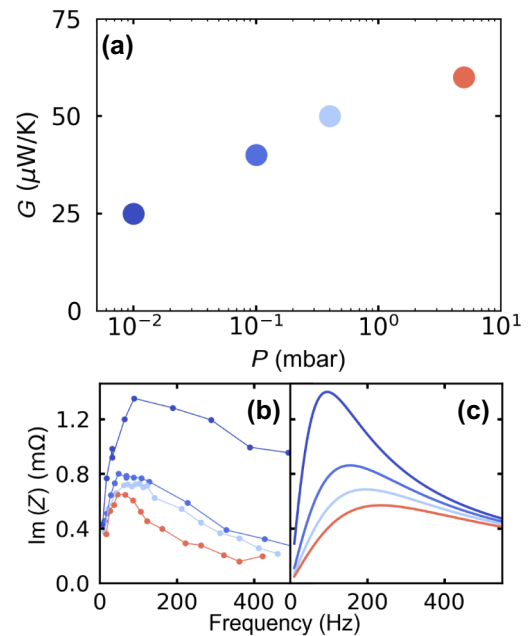


FIG. 3. (a) Curve of thermal conductance versus exchange-gas pressure deduced from Eq. (4). (b) Imaginary impedance as a function of frequency at about 7.2 K. The exchange-gas pressure varies from 0.01 to 5 mbar. The colors of the lines in (b),(c) correspond to the values shown in (a). (c) Results of the calculation described in the text using Eq. (4).

[Figs. 2(b), 2(e), and 2(h)] imaginary impedances as a function of the magnetic field and current, for vanishing residual exchange-gas pressure. Assuming that these differences are due just to the temperature variation of C in Eq. (4), we calculate C as a function of temperature. For this, we use the temperature dependence of $\text{Re}(Z)$ obtained from the experiment to numerically calculate $d\text{Re}(Z)/dT$. We compute $\text{Im}(Z)$ starting with a uniform ansatz curve for $C(T)$ and vary it numerically until we obtain the measured temperature dependence of $\text{Im}(Z)$. In Fig. 4, we show the result for three characteristic situations.

It is useful to discuss the $C(T)$ obtained together with the temperature dependence of the resistance and of its derivative. At zero magnetic field and with a small current [Fig. 4(a)], we observe that the resistance drops continuously with decreasing temperature. But $d\text{Re}(Z)/dT$ does not increase smoothly until it diverges at the transition, but instead shows a peak at approximately 7.15 K. This leads to a small peak in $C(T)$. The value that we find for C is comparable to the estimated heat capacity of our sample. Its temperature dependence is similar to that observed in the heat capacity of $2H\text{-NbSe}_2$ using macroscopic measurements. The heat capacity of the sample increases by the same amount in the temperature range shown in Fig. 4(a) [20,21]. The peak in C can be related to the peak in C at the superconducting transition and is of roughly the same order.

When a magnetic field is applied, the temperature range with a finite $d\text{Re}(Z)/dT$ inside the superconducting phase becomes considerably larger [Fig. 4(b)]. The peak in C also becomes larger. When a current is applied at zero magnetic field, [Fig. 4(c)], the peak in C becomes even larger, and there is a small but finite C over a substantial temperature range.

This temperature-independent C , well within the superconducting phase in the presence of a large current [at low temperatures in Fig. 4(c)], is quite remarkable. It corresponds roughly to the temperature range where $\text{Im}(Z)$ shows a broad maximum. Thus, there is a mechanism for heat production that develops in the presence of large currents well within the superconducting phase. This is related to vortex motion and the associated generation of quasiparticles.

First, we should realize that in Fig. 4(c) the temperature is close to T_c , and the current is above the critical current for the onset of vortex motion. In this range, the transition is very broad, and parameters such as α and β have a small and smooth temperature dependence. When a current is applied, vortices enter the sample. Vortices are pinned at defects and are mobile in between pinning centers in the presence of a current [22]. In this temperature range, and in the presence of such large currents, vortices are mobile. During vortex motion, the Lorentz force is compensated by a drag force that is dissipative [9,23–27]. Moving vortex cores requires transforming

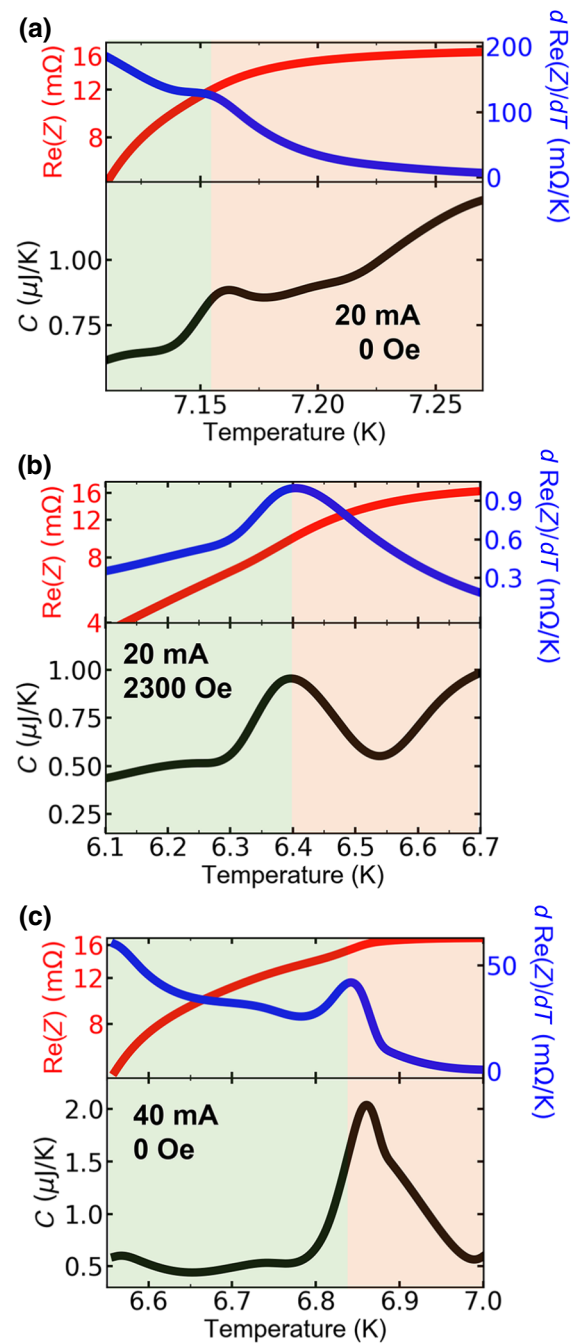


FIG. 4. The top panels of each part show the temperature dependence of the resistance (left y axis, red lines) and of dR/dT (right y axis, blue lines). The bottom panels show the value of C obtained as discussed in the text (black lines). Notice that the temperature range shown in each part corresponds to the range where the reactance is finite. (a) Results obtained at 10 mA and zero magnetic field [blue curves in Figs. 2(a) and 2(b)], (b) results obtained at 10 mA and 2300 Oe [orange curves in Figs. 2(a) and 2(b)], and (c) results obtained at 40 mA and zero magnetic field [orange curves in Figs. 2(d) and 2(e)]. The temperature range shaded green corresponds to the temperature region where at least part of the sample is superconducting, and the red shading corresponds to the normal region dominated by fluctuation and dissipation.

normal quasiparticles into Cooper pairs and produces out-of-equilibrium quasiparticles along their path [28]. At large driving currents, vortices move at very high velocities, even higher than the speed of sound [29–31]. They can be unstable at high driving velocities, leading to additional quasiparticles [29,32–36]. The observed increase in the imaginary impedance under a magnetic field shows the contribution from fluctuating vortices to the superconducting transition.

The value of C that we find is of the order of the electronic contribution to the specific heat capacity at zero current. Thus, the amount of excitations created by the current remains approximately constant in the temperature range where the real component of the impedance is finite, in spite of the strongly decreasing real impedance. The real impedance measures the voltage induced by current flow, which results from vortex motion between pinning centers. The imaginary impedance measures instead the heat created in this process.

IV. CONCLUSION AND OUTLOOK

In conclusion, we observe a strong mutual influence between heat and electronic transport in the superconducting transition of $2H$ -NbSe₂. The frequency for the appearance of the coupling is in the tens-of-hertz regime. We use a model that traces the behavior of the resistance back from the resistance, taking into account heating effects.

Our results suggest that measurements of both the real and the imaginary impedance are fundamental to determining the effect of temperature on a sharp superconducting transition. As we discuss in more detail in Appendix B, measurement of the imaginary impedance should be very useful for characterizing superconducting transitions, because it highlights overheating effects or the presence of residual exchange gas. More than that, as we show with the data as a function of current, it also provides precise information about the heat capacity of the sample. For example, a fundamental aspect of two-dimensional systems is the presence of out-of-equilibrium dissipation and coherence at the same time, as a consequence of a continuous Kosterlitz-Thouless type of transition into the normal state [12]. Very recent measurements suggest a thermally driven vortex blockade in ultrathin devices made of $2H$ -NbSe₂ [37]. Measurements of the critical current in $2H$ -NbSe₂ contacted with graphene show strongly reduced values with respect to a metallic electrode, suggesting that electron flow in the graphene generates heat that is transferred to the $2H$ -NbSe₂ [38]. These measurements consider only the real impedance, which shows just electronic transport. The imaginary impedance should be much larger in thin films in the limit of small currents than we observe here, and can serve as an alternative method to characterize thermal behavior in these and similar systems.

Our results also show a highly nonlinear effect of the exchange gas (Fig. 3). The measured dependence of the thermal conductance G due to mass flow (convection) of a gas in a vacuum as a function of the pressure shows a similar increase to what we observe here [19,39]. The order of magnitude of G corresponds to a distance of the order of 1 cm, which is comparable to the size of our setup. Recent measurements of dissipation in quantum systems have been made by connecting a temperature sensor to the sample through exchange gas [40,41]. The measurement of the real and imaginary components of the resistive superconducting transition can be used to independently characterize this link.

One might expect at first sight that thermal effects are just a consequence of having a sharp transition. Our work shows that the broadening of the transition on application of a current does not lead to a vanishing imaginary component. We reveal a strong increase in the imaginary impedance when large currents are applied. This increase is due to an additional contribution to the specific heat capacity from the quasiparticles generated during vortex motion.

ACKNOWLEDGMENTS

This work was supported by the Spanish Research State Agency (Grants No. FIS2017-84330-R and No. MAT2017-89993-R; and the “Maria de Maeztu” programme for units of excellence.No. MDM-2015-0538 and No. CEX2018-000805-M) and by the Comunidad de Madrid through program NANOMAGCOST-CM (Grant No. S2018/NMT-4321). I.G. and E.C. acknowledge support from the European Research Council (Grants No. 679080 (I.G., PNICTEYES) and No. 788222 (E.C. MOL-2D)). We also acknowledge the EU COST program NANOCOBYBRI (Grant No.:CA16218) and the SEGAINVEX at UAM. We thank R. Álvarez Montoya for technical support, and A. García and D. Caldevilla for support at the beginning of the project. We also thank Andrey Varlamov, A.I. Buzdin, and J.C. Cuevas for enlightening discussions.

APPENDIX A: IMAGINARY IMPEDANCE VERSUS FREQUENCY

We present here a measurement of the impedance at a fixed temperature while the frequency is varied. To obtain the green line in Fig. 5, we use $C = 2.6 \times 10^{-7}$ J/K, $G = 9.5 \times 10^{-5}$ W/K, $\alpha = 102$, and $\beta = 69$, which are the values obtained by fitting the imaginary part of the impedance with Eq. (4). The heat capacity C of our sample can be estimated from the sample size ($1.6 \text{ mm} \times 0.8 \text{ mm} \times 14 \text{ }\mu\text{m}$) and the molar heat capacity of $2H$ -NbSe₂, 400 mJ/(mol K) [20]; we obtain $C \approx 1.7 \times 10^{-7}$ J/K. With the value of G used, we can estimate the value of dT produced by the Joule power in the sample, and obtain about 20 mK. Using

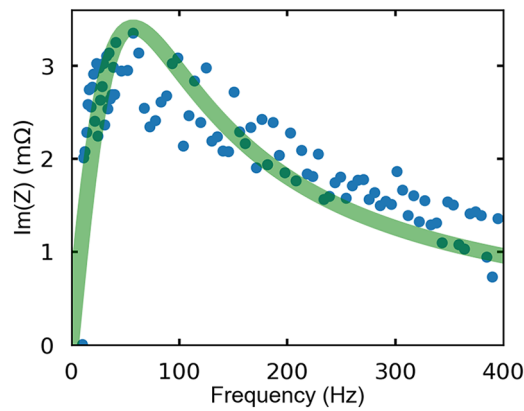


FIG. 5. The blue points show the reactance versus frequency, and the fit to the model described in the text is shown in green. The measurement temperature is 7.2 K, and the exchange-gas residual pressure is below 0.01 mbar.

α , we can again estimate dT , and obtain approximately the same value. The α and β obtained are compatible with the usual values at the transition in $2H\text{-NbSe}_2$. The agreement between the calculations and experiment (Fig. 5) and the values obtained for the different parameters show that the linearized equations account well for the behavior obtained over a large part of the superconducting transition.

APPENDIX B: COMMENTS ON THE MEASUREMENT OF THE RESISTIVE TRANSITION

Our results imply that the resistive transition cannot be understood solely on the basis of measurements of the real impedance. The resistive transition of superconductors has been studied in depth in the limit of vanishing current, or when heat dissipation in the sample can be neglected [7,8,42,43]. The discussion has focused on the influence of fluctuations on the conductivity. When the transition is approached from higher temperatures, fluctuations modify the conductance gradually from the normal-state value until it diverges at some point. The temperature range for the influence of fluctuations on the thermodynamic properties is approximately given by $(T - T_c)/T_c > G_L$ (where G_L is the Ginzburg-Levanyuk number [8]), which is practically negligible for $2H\text{-NbSe}_2$ [44]. However, in the conductivity, fluctuations appear much earlier due to non-linear effects, at about $(T - T_c)/T_c > \sqrt{G_i}$, which leads to a temperature range that can cover a few tens of millikelvin [45]. Indeed, at the smallest currents, we observe that the resistance starts to drop at a few tens of millikelvin before the actual transition. Several different contributions might modify the conductivity at zero magnetic field and zero frequency around the superconducting transition in a superconductor. First, strongly time-dependent fluctuations in the superconducting order parameter might lead, when

averaged over time, to bubbles with higher conductance due to time-fluctuating preformed Cooper pairs; this is termed the Aslamazov-Larkin contribution [8]. Second, the normal-state density of states might already show a dip above T_c [8]. Third, the Maki-Thompson contribution, due to the formation of Cooper pairs at self-interfering trajectories caused by scattering at impurities, might modify the conductivity [46–48]. In the clean limit (i.e. when the mean free path ℓ is much larger than the superconducting coherence length ξ), only the Aslamazov-Larkin contribution is relevant, and this leads to the observed decrease in the resistance above T_c . Our results show that there is an imaginary impedance that has remained unnoticed in the fluctuation range. The result at low current and zero magnetic field seems to follow well the specific heat capacity of the sample, suggesting that these mechanisms make a minor contribution to the heat balance in the sample. However, this changes when a magnetic field or a current is applied, as we discuss in the main text.

On more experimental grounds, we should note that the imaginary impedance appears at low frequencies and thus in transport experiments that are not done exactly under dc conditions. All kinds of electronic measurement imply a change in the parameters with time, either to remove thermoelectric voltages in the usual four-wire measurement [49,50] or simply to vary the temperature in regular steps. Through the power used to perform the measurement, there is a connection between the resistance and the temperature, which induces a reactance when the resistance is strongly temperature-dependent.

-
- [1] K. Irwin and G. C. Hilton, in *Cryogenic Particle Detection*, Topics Appl. Phys. Vol. 99 (Springer – Verlag, Berlin-Heidelberg-New York, 2005). 1st ed.
 - [2] J. N. Ullom and D. A. Bennett, Review of superconducting transition-edge sensors for X-ray and γ -ray spectroscopy, *Supercond. Sci. Technol.* **28**, 084003 (2015).
 - [3] D. Redfern, J. Nicolosi, J. Höhne, R. Weiland, B. Simmnacher, and C. Hollerich, The microcalorimeter for industrial applications, *J. Res. Natl. Inst. Stand. Technol.* **107**, 621 (2002).
 - [4] R. C. Jones, The general theory of bolometer performance, *J. Opt. Soc. Am.* **43**, 1 (1953).
 - [5] J. E. Vaillancourt, Complex impedance as a diagnostic tool for characterizing thermal detectors, *Rev. Sci. Instrum.* **76**, 043107 (2005).
 - [6] M. Galeazzi and D. McCammon, Microcalorimeter and bolometer model, *J. Appl. Phys.* **93**, 4856 (2003).
 - [7] A. V. Anatoly Larkin, *Theory of Fluctuations in Superconductors*, International Series on Monographs in Physics Vol. 127 (Oxford University Press, Oxford, UK, 2009).
 - [8] A. A. Varlamov, A. Galda, and A. Glatz, Fluctuation spectroscopy: From Rayleigh-Jeans waves to Abrikosov vortex clusters, *Rev. Mod. Phys.* **90**, 015009 (2018).

- [9] A. Schmid, A time dependent Ginzburg-Landau equation and its application to the problem of resistivity in the mixed state, *Physik der kondensierten Materie* **5**, 302 (1966).
- [10] A. Schmid and G. Schon, Linearized kinetic equations and relaxation processes of a superconductor near T_c , *J. Low Temp. Phys.* **20**, 207 (1975).
- [11] J. Clarke, Experimental Observation of Pair-Quasiparticle Potential Difference in Nonequilibrium Superconductors, *Phys. Rev. Lett.* **28**, 1363 (1972).
- [12] Y. Chen, Y.-H. Lin, S. D. Snyder, A. M. Goldman, and A. Kamenev, Dissipative superconducting state of non-equilibrium nanowires, *Nat. Phys.* **10**, 567 (2014).
- [13] M. Naito and S. Tanaka, Electrical transport properties in 2H-NbS₂, -NbSe₂, -TaS₂ and -TaSe₂, *J. Phys. Soc. Jpn.* **51**, 219 (1982).
- [14] A. Maldonado, S. Vieira, and H. Suderow, Supercurrent on a vortex core in 2H-NbSe₂: Current-driven scanning tunneling spectroscopy measurements, *Phys. Rev. B* **88**, 064518 (2013).
- [15] M. A. Lindeman, S. Bandler, R. P. Brekosky, J. A. Chervanek, E. Figueroa-Feliciano, F. M. Finkbeiner, M. J. Li, and C. A. Kilbourne, Impedance measurements and modeling of a transition-edge-sensor calorimeter, *Rev. Sci. Instrum.* **75**, 1283 (2004).
- [16] E. Taralli, C. Portesi, L. Lolli, E. Monticone, M. Rajteri, I. Novikov, and J. Beyer, Impedance measurements on a fast transition-edge sensor for optical and near-infrared range, *Supercond. Sci. Technol.* **23**, 105012 (2010).
- [17] V. V. E. Schmidt, in *The physics of superconductors: Introduction to fundamentals and applications* (Springer Science & Business Media, 2013).
- [18] K. Takita and K. Masuda, Charge density wave transition and superconductivity in 2H-NbSe₂. Direct measurement of the penetration depth in a layered superconductor, *J. Low Temp. Phys.* **58**, 127 (1985).
- [19] D. Ganta, E. Dale, J. Rezac, and A. Rosenberger, Optical method for measuring thermal accommodation coefficients using a whispering-gallery microresonator, *J. Chem. Phys.* **135**, 084313 (2011).
- [20] C. L. Huang, J.-Y. Lin, Y. T. Chang, C. P. Sun, H. Y. Shen, C. C. Chou, H. Berger, T. K. Lee, and H. D. Yang, Experimental evidence for a two-gap structure of superconducting NbSe₂ specific-heat study in external magnetic fields, *Phys. Rev. B* **76**, 212504 (2007).
- [21] E. Boaknin, M. A. Tanatar, J. Paglione, D. Hawthorn, F. Ronning, R. W. Hill, M. Sutherland, L. Taillefer, J. Sonier, S. M. Hayden, and J. W. Brill, Heat Conduction in the Vortex State of NbSe₂: Evidence for Multiband Superconductivity, *Phys. Rev. Lett.* **90**, 117003 (2003).
- [22] G. Blatter, M. V. Feigel'man, V. B. Geshkenbein, A. I. Larkin, and V. M. Vinokur, Vortices in high-temperature superconductors, *Rev. Mod. Phys.* **66**, 1125 (1994).
- [23] Y. B. Kim, C. F. Hempstead, and A. R. Strnad, Flux-flow resistance in type-II superconductors, *Phys. Rev.* **139**, A1163 (1965).
- [24] K. Maki, Vortex motion in superconductors, *Physica* **55**, 124 (1971).
- [25] J. Bardeen and M. J. Stephen, Theory of the motion of vortices in superconductors, *Phys. Rev.* **140**, A1197 (1965).
- [26] C.-R. Hu and R. S. Thompson, Dynamic structure of vortices in superconductors. II. $H \ll H_c2$, *Phys. Rev. B* **6**, 110 (1972).
- [27] J. R. Clem, Local Temperature-Gradient Contribution to Flux-Flow Viscosity in Superconductors, *Phys. Rev. Lett.* **20**, 735 (1968).
- [28] V. G. Kogan, Time-dependent London approach: Dissipation due to out-of-core normal excitations by moving vortices, *Phys. Rev. B* **97**, 094510 (2018).
- [29] L. Embon, Y. Anahory, Z. L. Jelic, E. O. Lachman, Y. Myasoedov, M. E. Huber, G. P. Mikitik, A. V. Silhanek, M. V. Milosevic, A. Gurevich, and E. Zeldov, Imaging of superfast dynamics and flow instabilities of superconducting vortices, *Nat. Commun.* **8**, 85 (2017).
- [30] G. Grimaldi, A. Leo, P. Sabatino, G. Carapella, A. Nigro, S. Pace, V. V. Moshchalkov, and A. V. Silhanek, Speed limit to the abrikosov lattice in mesoscopic superconductors, *Phys. Rev. B* **92**, 024513 (2015).
- [31] O. Dobrovolskiy, V. Bevz, E. Begun, R. Sachser, R. Vovk, and M. Huth, Fast Dynamics of Guided Magnetic Flux Quanta, *Phys. Rev. Appl.* **11**, 054064 (2019).
- [32] F. Estellés-Duart, M. Ortuño, A. M. Somoza, V. M. Vinokur, and A. Gurevich, Current-driven production of vortex-antivortex pairs in planar Josephson junction arrays and phase cracks in long-range order, *Sci. Rep.* **8**, 15460 (2018).
- [33] Z. Jing, H. Yong, and Y. Zhou, Thermal coupling effect on the vortex dynamics of superconducting thin films: Time-dependent ginzburg-landau simulations, *Supercond. Sci. Technol.* **31**, 055007 (2018).
- [34] M. Leroux, F. F. Balakirev, M. Miura, K. Agatsuma, L. Civale, and B. Maiorov, Dynamics and Critical Currents in Fast Superconducting Vortices at High Pulsed Magnetic Fields, *Phys. Rev. Appl.* **11**, 054005 (2019).
- [35] B. Kalisky, P. Aronov, G. Koren, A. Shaulov, Y. Yeshurun, and R. P. Huebener, Flux-Flow Resistivity Anisotropy in the Instability Regime of the a-b Plane of Epitaxial Superconducting YBa₂Cu₃O₇ Thin Films, *Phys. Rev. Lett.* **97**, 067003 (2006).
- [36] M. N. Kunchur, D. K. Christen, C. E. Klabunde, and J. M. Phillips, Pair-Breaking Effect of High Current Densities on the Superconducting Transition in YBa₂Cu₃O₇, *Phys. Rev. Lett.* **72**, 752 (1994).
- [37] A. Benyamini, D. M. Kennes, E. Telford, K. Watanabe, T. Taniguchi, A. Millis, J. Hone, C. R. Dean, and A. Pasupathy, Blockade of vortex flow by thermal fluctuations in atomically thin clean-limit superconductors, arXiv:1909.08469 [cond-mat.mes-hall] (2019).
- [38] Y. Sata, R. Moriya, N. Yabuki, S. Masubuchi, and T. Machida, Heat transfer at the van der Waals interface between graphene and NbSe₂, *Phys. Rev. B* **98**, 035422 (2018).
- [39] T. Funke and C. Haberstroh, *New measurements of multi-layer insulation at variable cold temperature and elevated residual gas pressure*, IOP Conference Series: Materials Science and Engineering, Vol. 101 (IOP Publishing, Tucson, AZ, USA, 2015).
- [40] D. Halbertal, J. Cuppens, M. B. Shalom, L. Embon, N. Shadmi, Y. Anahory, H. R. Naren, J. Sarkar, A. Uri, Y. Ronen, Y. Myasoedov, L. S. Levitov, E. Joselevich,

- A. K. Geim, and E. Zeldov, Nanoscale thermal imaging of dissipation in quantum systems, *Nature* **539**, 407 (2016).
- [41] D. Halbertal, A. Uri, K. Bagani, A. Y. Meltzer, I. Marcus, Y. Myasoedov, E. Zeldov, M. B. Shalom, J. Birkbeck, A. K. Geim, and L. S. Levitov, Imaging resonant dissipation from individual atomic defects in graphene, *Science* **358**, 1303 (2017).
- [42] J. R. Miller and J. M. Pierce, Fluctuation effects in the complex impedance of superconducting tin-whisker crystals near T_c , *Phys. Rev. B* **8**, 4164 (1973).
- [43] A. Kremen, H. Khan, Y. L. Loh, T. I. Baturina, N. Trivedi, A. Frydman, and B. Kalisky, Imaging quantum fluctuations near criticality, *Nat. Phys.* **14**, 1205 (2018).
- [44] A. I. Larkin and A. A. Varlamov, in *Superconductivity: Conventional and Unconventional Superconductors*, edited by K. H. Bennemann and J. B. Ketterson (Springer Berlin Heidelberg, Berlin, Heidelberg, 2008), p. 369.
- [45] A. I. Larkin and Y. N. Ovchinnikov, Nonlinear fluctuation phenomena in the transport properties of superconductors, *J. Exp. Theoretical Phys.* **92**, 519 (2001).
- [46] K. Maki, The critical fluctuation of the order parameter in type-II superconductors, *Prog. Theor. Phys.* **39**, 897 (1968).
- [47] R. S. Thompson, Microwave, flux flow, and fluctuation resistance of dirty type-II superconductors, *Phys. Rev. B* **1**, 327 (1970).
- [48] C. Carballeira, J. Mosqueira, A. Revcolevschi, and F. Vidal, First Observation for a Cuprate Superconductor of Fluctuation-Induced Diamagnetism Well inside the Finite-Magnetic-Field Regime, *Phys. Rev. Lett.* **84**, 3157 (2000).
- [49] A. L. Pope, R. T. Littleton IV, and T. M. Tritt, Apparatus for the rapid measurement of electrical transport properties for both “needle-like” and bulk materials, *Rev. Sci. Instrum.* **72**, 3129 (2001).
- [50] Quantum Design, *Physical Property Measurement System: Resistivity Option User’s Manual*, PPMS Manual (1999).